SM1: Data sources on rockfall activity

The tittle of this paper appeals to multi-source data on rockfall activity. In section 1.2 these sources are shortly mentioned, before focusing on monitoring and inventory, being the data sources for the included site cases. Given the difficulty in most cases in having enough data in quantity and quality to establish the McF pattern, the solution is based on being able to combine, or at least contrast, all available sources at different scales. And the methods of optimizing its exploitation presented in section 4 can be applied similarly. In this appendix, these other possible sources of information and their attributes are detailed a little more:

- Event observation:
  - Direct observation by technicians, who are carrying out local surveillance for risk mitigation purposes at local scale (e.g., infrastructure-based) that includes inventory task (1,2).
  - Observation by affected person or witness, who remember the facts or write them down in private annotations. Information is preserved in individual or collective memory and can be retrieved by survey to local people. The more relevant the fact, the easier it is to last over time (3).
  - Observation by non-residents on the site, usually in the open air and without affecting human facilities. If citizen science projects are taking place, the witness can report the event with the required information for so-prepared inventories (4–6).
- Documentary record:
  - When the event causes relevant affectations, it is possible that a written record remains, typically focused on the caused damage, from which information should be inferred the event attributes not directly reported. This information can be very scattered in socio-economic archives, newspaper archives, local monographs or others that are rarely digitized and even less available online (7,8).
- Land photographic register:
  - The orthophotographic series produced by public agencies constitute a graphic record from which activity can be interpreted for events of sufficient magnitude to be visible at the working scale (9).
  - Photographs of very diverse formats and sources that, without pretending to immortalize a state of the landscape at a certain moment, by repetition, record a temporal evolution. Society is currently taking a huge number of pictures that are also globally accessible thanks to the internet and social networks. This resource can be particularly productive in mountainous areas of high landscape value and touristic frequentation (10).
- Remote sensing:
  - Some monitoring techniques allow the recording of rockfall activity, although instrumental systems are not specially designed for this purpose, such as LiDAR or photogrammetry, either with continuous devices or with periodic surveys (11).
  - Seismic monitoring networks also record the signal of large landslides and, if identified, they can be accurately dated (12,13).

It is necessary to consider the limitations of the data capturing method to be compensated when processing the information for frequency assessment (see Figure S1).

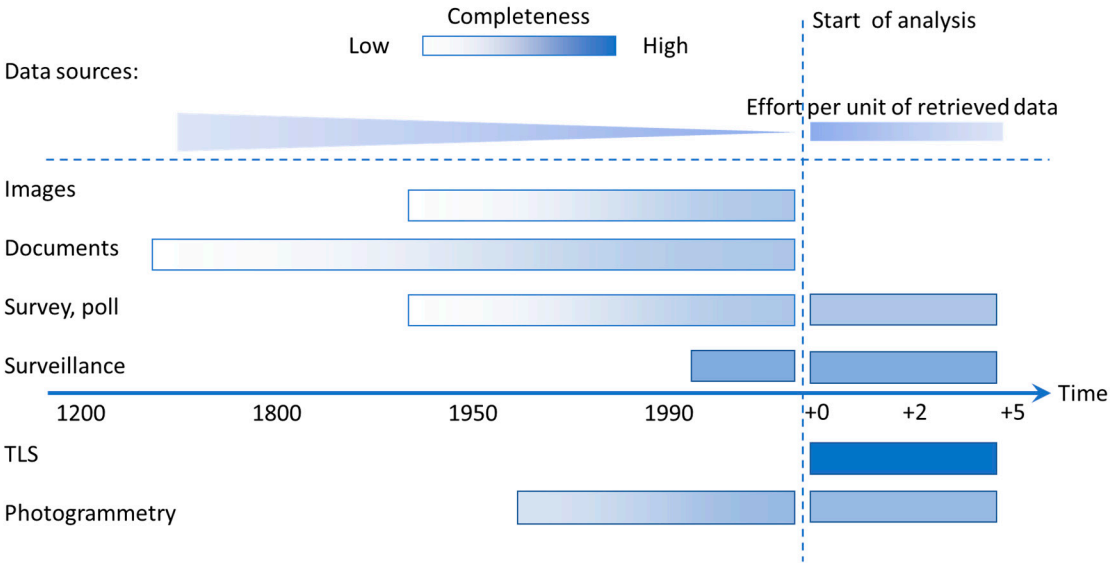

Figure S1. Symbolic diagram of the common sources of information on rockfall activity applied to the case sites in this article. The degree of completeness expected in each case is qualitatively indicated. The effort required per unit of information obtained increases when going back into the past.

To deal with the reconstruction of past activity, a complementary task to the inventory is the recognition of signs of landslide activity on the ground. Although they are generally partial indications of the events (e.g., a waypoint, a fragment or part of the deposit), they sometimes allow events to be reconstructed in their total volume, or they provide complementary dates to the inventory. Among the techniques of dating clues, we can cite in the sense of rock fall trajectory:

- The dating by cosmogenic nuclides or by colorimetry of the scars on the rock wall (14,15).
- Dendrochronology applied to impacts on the trees and effects on the forest (16,17).
- Lichenometry or optically stimulated luminescence applied to seen faces and buried faces of fallen blocks deposited on slopes and scree (18,19).

Those methods dating the scars on the wall will be closer to our analysis purpose in terms of the detachment size form the starting zone. (20,21) proposed an erosion model that relates rockfall frequency, rock wall retreat rate and rock surface exposure age given by cosmogenic nuclides. For an extended review of methods used for landslide dating refer to (22).

SM2: Power law for McF

A power law like $F_{st}(V) = A_{st} \cdot V^{-B}$ introduced in section 2.1 is a hyperbolic function in natural scale and a linear function in logarithmic scale for both variables (see Figure S2). $F_{st}(V)$ is a uniformly decreasing function on the V axis, as it corresponds to its meaning of inverse cumulative frequency. The slope of the hyperbola (first derivative) is a uniformly increasing function with $\lim_{V \to 0^+} F'_{st} = -\infty$ and $\lim_{V \to +\infty} F'_{st} = 0$. We define the center of the hyperbola as the point where the curve F_{st} is orthogonal to the direction of the bisector line of the first quadrant ($F'_{st} = -1$). This center is placed on the volume value $V_c = (A_{st} \cdot B)^{1/(B+1)}$ and its frequency is $F_c = A_{st}(A_{st} \cdot B)^{-B/(B+1)}$. By definition, on the left side of V_c frequency decreases quicklier than volume increases, and on the right side of V_c frequency decreases slower than volume increases.

On natural scale (see Figure S2), parameter B is related to the angular position of the hyperbola's center and its distance from bisector line, being the singular case of $B = 1$ the perfect symmetry, and the common case of $B < 1$ the

tilt to lower volumes, what magnifies the separation of the curve from the abscissa axis for largest volumes compared to the distance of the lowest volumes branch of the curve from ordinate axis. $B > 1$ implies the asymmetry in the opposite sense. In conclusion, both parameters A_{st} and B define the polar coordinates of the hyperbola's center and the shape is fixed by the unitary slope at the center and the asymptotic tangency to both axes. On logarithmic scale (see Figure S2) and with both variables as positive real numbers $\{V; F_{st}\} \in \mathbb{R}^+$, A_{st} is the independent term in ordinate of the straight line and B is its slope. This is the common representation for these relationships assuming fractal behavior and the easiest way to analyze power law fitting.

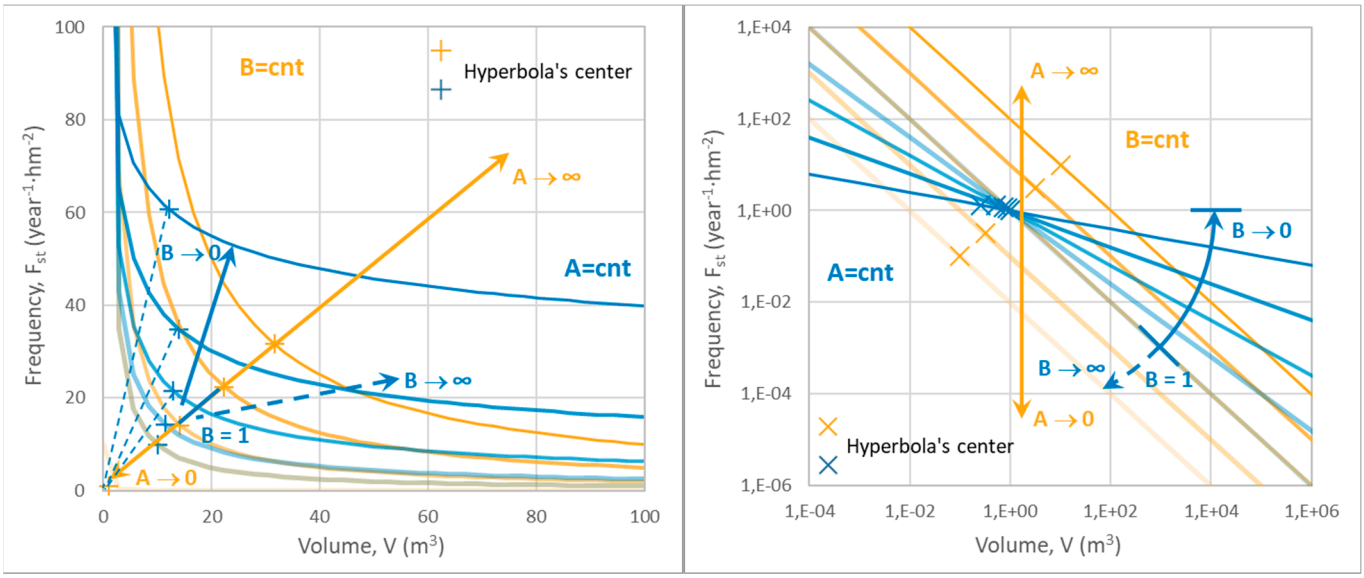

Figure S2. Theoretical curves of power law function for spatio-temporal frequency of rockfall magnitude $F_{st}(V) = A_{st} \cdot V^{-B}$ in natural scale (left) and logarithmic scale (right). The role of both parameters A_{st} and B is shown, when a constant value for eighter A_{st} (blue) or B (orange) is maintained to show the influence of the other one. The position of hyperbola's center is highlighted for each curve. For greater clarity of the figure, examples with $B > 1$ have not been included and their trend has been indicated with dashed line.

As stablished by (23), integration of the area below the hyperbola corresponds to the erosion rate as descriptor of the detachment hazard of the outcrop. It should be noted that for the common case of $B \leq 1$ a maximum value of volume must be set to converge integration, what is coherent with the idea that there is a physical limit for magnitude, according to the slope geometry and structural conditions (24). Equivalently, when $B \geq 1$ a lower limit for volume must be set, avoiding the senseless cases of micro-detachments that, spite being of very small dimensions, their frequency mathematically was so high to diverge erosion rate. It can be said that in the first case morphology is determined by major events, while in the second case is the continuous erosion who plays determinant action. Finally, when $B \approx 1$ both thresholds are necessary, as integral function approaches to the function $\ln(V)$. Once erosion rate is determined this way, hazard can be calculated for every outcrop both as retreat at the top (in $mm/year$ of mean retreat) and the mass flow of rockfalls at the bottom (in $m^3/year$ of rockfall activity). This analysis is out of the scope of this paper and will be performed for case sites in the next future.

The contribution of its center to hazard level is the product of both coordinates $p_c = V_c \cdot F_c = A_{st}(A_{st} \cdot B)^{\frac{1-B}{1+B}}$. The distance of the center to the coordinate origin is $d_c = V_c\sqrt{1+\frac{1}{B^2}} = (A_{st} \cdot B)^{1/(B+1)}\sqrt{1+\frac{1}{B^2}}$ and it is not necessarily the minimum value of the F_{st} curve. Instead, we define the origin of the hyperbola as the point closest to coordinate origin

(0,0). This origin is placed on the volume value $V_0 = (A_{st}^2 \cdot B)^{1/2(B+1)}$ and its minimum distance to origin is $d_0 = V_0\sqrt{1+\frac{1}{B}} = (A_{st}^2 \cdot B)^{1/2(B+1)}\sqrt{1+\frac{1}{B}}$.

For the singular case of $B = 1$, the hyperbola is symmetric respect to the bisector and both its center and origin are coincident $(V_0 = V_c)$ and are placed on this line with $V_c = F_c = \sqrt{A_{st}}$, and consequently $d_c = \sqrt{2A_{st}}$ and $p_c = V_c \cdot F_c = A_{st}$. For a generic value of B, A_{st} is also related to this distance that can be observed on natural scale with the limit case of $A_{st} \to 0$, when the curve collapses to the axis and $F_{st}(V) = 0$ for all volume range, corresponding to the absence of activity and hazard.

Finally, it is worth noting that not only event inventories respond to a power law for the total volume in the starting zone, but also the distribution of deposited blocks volumes in the arrival zone are adequately described by similar distributions according to several authors (25–27). For this case, a slight modification of the parameters notation is proposed by (23) to distinguish both size distributions, adopting lowercase letters: $F(V_{fb}) = a \cdot {V_{fb}}^{-b}$, and using V_{fb} we can emphasize that the volume of fragmented blocks is considered in this case. Comparison of both coefficients, B and b, reveals the fragmentation process of falling rocks including the initial disaggregation and the breakage during the propagation (28). As only fragmentation of large blocks and no aggregation of small blocks occur in rockfall, it can be seen that $B \leq b$.

Using the sampling extent SE introduced in the paper, F_{st} is normalized twice: spatially and temporally. On the one hand, covered time calculation is physically unambiguous, despite uncertainty arises mostly for historical inventories. As a result, additional considerations are set out later for temporal normalization in observational inventories, what provide the meaning of frequency according to recurrency. On the other hand, we go deeper in detail on spatial normalization since surface measurement can become ambiguous. Thanks to high resolution of 3D models obtained by remote sensing techniques like TLS, precise measurement of the rock face area can be achieved. But we could fall into an uncertainty equivalent to that of the coastline length: the greater the detail on the roughness of the rock surface, the greater the area obtained. As we are focused on erosion rate or escarpment retreat computation, the surface to be measured as reference is orthogonal to that direction. Detailed roughness is not representative of the rock mass providing rockfall activity. Consequently, we take the measurement in a 2.5D model that basically considers the height and verticality of the wall. From the terrain elevation model, we calculate the developed pixel area by applying the factor $1/\cos\theta$ on the planimetric area of the grid cell, being θ the slope angle provided that is greater than a threshold to be considered as source for rockfall. In this way, the measurement of the reference surface can be homogeneous between the places with TLS monitoring and those of the inventory, where no 3D models are not available.

SM3: Test sites features

The test sites in this paper are pioneering cases in Catalonia, and even in Spain, in the use of TLS monitoring applied to rockfall hazard, together with Núria Valley in the Pyrenees and Puigcercós ancient village in the Ebro basin foreland (29–31). The first LiDAR scanner on rock slope was taken in 2003 by ICGC in Núria for the hazardous section of the rack railway that finally was by-passed by a tunnel, but a monitoring program has not been continued since then. The longest monitoring series available by ICGC is given in the Montserrat Massif, corresponding to the Degotalls wall and initiated after a large rockfall occurred in 2007. Table S1 summarizes a comparative overview of these test sites. It is worth noting that they have allowed a chain of fruitful doctoral theses (32–35) in remote sensing applications to rockfall.

Table S1. Summary of the four pioneering test sites of LiDAR applications to rockfall hazard analysis in Catalonia. ISRM basic description of rock masses is according to (36), where L_i is the layer thickness and F_i is the fracture intercept.

	Montserrat Massif	Núria Valley	Castellfollit de la Roca	Puigcercós
Rock mass (lithology)	Conglomerate interleaved by siltstones	Gneiss	Basalt	Alternation of marls, sandstone, silt- and claystone
Rock mass (structure)	Fractures of large persistence and spacing and sub- horizontal bedding	Fractures, faults, foliation	Two overlayed lava flows levels, columnar disjunction	Fractured rock mass, extensional slabs and subhorizontal bedding
Rock mass (ISRM descriptors)	$L_{1,2}$ $F_{1,2}$	L_1 $F_{2,3}$	$L_{2,3}$ F_2	L_3 F_3
Geological context	South margin of Ebro basin	Pyrenees	Catalan Transversal range	North margin of Ebro basin
Relief and geodynamics	Rock needles and walls in stepped slope	Glacio-fluvial valley, steep slopes and gorges	River side cliff	Scar of ancient landslide (in 1881)
Outcrop surface (hm^2)	1000 hm^2 (natural park)	100 hm^2 (rack railway)	5 hm^2	0.5 hm^2
Elevation (m.a.s.l.)	200 – 1200	1200 – 2000	240 – 295	425 – 550
Predominant aspect	All	E & W	N & S	SW
Environmental Context	Mid mountain	High mountain	Low mountain	Hills and plains
Climatic conditions	Torrential Mediterranean climate	Wet-Mediterranean mountain climate	Wet-Mediterranean climate	Dry-Mediterranean climate
Annual mean precipitation (mm)	700 (Autumn-Spring)	1100 (Summer-Autumn)	950 (Summer-Spring)	650 (Spring-Autumn)
Annual mean temperature (ºC)	11	6	13	12
Mean range of temperature (ºC)	16	14	17	20
Seismic zone (MSK intensity for T500)	VI	VII-VIII	VII-VIII	VII
Elements at Risk	Buildings, roads, rack railway	Rack railway	Town	Castle ruins (abandoned village)
First TLS survey	May 2007	September 2003	March 2006	October 2007

Parallelly, Castellfollit de la Roca was the first of these cases where rock face deformation was detected by TLS monitoring and studied as rockfall precursor (37), thanks to a 50 m^3 rockfall in 2007 and the progressive toppling mechanism of basalt columns. The complete list of rockfalls included in the observational inventory is shown in Table S2. It remains a test site at present for a permanent photogrammetric system, which is not the subject of this paper (38,39), but it will provide interesting complementary data about rockfall activity, dating and precursory signs.

Table S2. List of the 19 rockfall registered in the observational inventory until 2020 in Castellfollit de la Roca cliffs. It is pointed out that two rockfalls are also registered by TLS monitoring in this study.

Volume (m^3)	When? (year)	Where? cliff	Observations
1500	1976	North (Fluvià)	
960	1976	North (Fluvià)	
850	2011	North (Fluvià)	
75	2017	South (Turonell)	
60	2015	South (Turonell)	

50	1995	North (Fluvià)	
50	2007	North (Fluvià)	
6,0	2019	North (Fluvià)	TLS overlap
5	2006	South (Turonell)	
5	2009	South (Turonell)	
5	2018	South (Turonell)	
3,7	2020	North (Fluvià)	TLS overlap
3	2008	North (Fluvià)	
3	2010	South (Turonell)	
3	2015	South (Turonell)	
2	2006	North (Fluvià)	
1,5	2006	South (Turonell)	
1,5	2010	South (Turonell)	
1	2005	South (Turonell)	

SM4: Rockfall activity mapping

Hazard assessment oriented to land use planning needs to communicate results to an interdisciplinary work team. Different formats for the representation of rockfall activity have been tested aimed at this purpose.

On the one hand, density maps of activity on the walls can be obtained from this information, at which different symbolization criteria can be applied (40). These visualizations highlight past activity; therefore, any confusion about where to expect future activity should be avoided. This perception could be valid in situations of rupture propagation with sequential falls, and it can take profit of presenting together both types of precursory indicators over time: precursory rockfalls and pre-failure deformation (41). But in general conditions of diffuse risk, it should be avoided to lead stakeholders to the error of perceiving the absence of hazard in sectors where no recent activity has occurred, but rockfalls may being prepared for the near future.

On the other hand, purely descriptive information on the location where rockfalls have been detected can take advantage of the communicative power of the 3D models obtained by the TLS monitoring together with new technologies that make 3D visualization accessible. Web viewers can overcome the barrier of the need for the user to have locally available this kind of voluminous data and specific software. For the application cases presented here, point cloud web viewers have been enabled based on the Potree open-source code (42). For example, the Montserrat Massif viewer [https://visors.icgc.cat/nuvols-punts-3d/montserrat-despreniments-tls/] shows the centroids of the detected rockfalls, and the Castellfollit de la Roca viewer [https://visors.icgc.cat/nuvols-punts-3d/castellfollit-despreniments-tls/] shows the clusters of the detected rockfalls, which expresses their volume (43). Finally, it is worth mentioning the new possibilities offered by mixed reality technologies in communicating this information of 3D nature from environments that are difficult to access such as the rocky walls in natural slopes to make them comprehensible to any kind of stake holders (44).

SM5: Hazard mitigation effectiveness

As said in section 5.2, rockfall activity can be also modified by works on the wall, as is his intention, both clearing of blocks of precarious stability and stabilization of potentially unstable masses. An example where this effect can be observed is the rack railway. This infrastructure was inaugurated in 2003 after two years of reconstruction works that acted intensively in clearance and stabilization due to the lesson learnt from the effects observed during the flash flooding on June 10th 2000, which caused a high degree of landslide activity (slides, flows and rockfall) all over the mountain. After the rockfall episode of Degotalls, a second work campaign was carried out to complete a continuous defense with barriers. At the time, a qualitative assessment was made of the reduction in hazard achieved (45). Now, monitoring with TLS would give us the possibility of making a quantitative assessment.

In this case example, we are faced with the hindrance of having only two monitoring sectors (Guilleumes and Sant Benet), the ones with the smallest sampling extent ($SE < 5hm^2 \cdot year$), and missing sample of the previous period to be compared directly. In addition, its limited representativeness does not allow us to identify a sector without intervention with an equivalent natural behavior with which to make the contrast.

To overcome this limitation with available TLS sample, inventory offers data enough to allow us making a first assessment exercise of the change in hazard provided by mitigation. In the temporal distribution of rockfalls (Figure S3) we observe no occurrence of events larger than 10 m³ since 2002 anywhere along the track of 2.8 km length exposed to 30.2 hm² of source area, even though 3 had occurred within the ten years prior to the works.

The frequency of rockfalls decreases strongly with the volume, and thus it is reflected in the McF obtained from the inventory with $B = 0.78$ (Table 6 in the paper) clearly higher than the average adjustments in the massif, and $A_{st} = 0.029$ being a value in the lower part. In contrast, if we consider that for this volume range from 10 to 1000 m³ there has been a human intervention that has prevented rockfalls, and consequently we extract this part of SE in the calculation we obtain a McF with $A_{st} = 0.047$ and $B = 0.60$. The difference between the 2 models implies that the frequency of rockfalls greater than 100 m³ (those that have the potential to overcome the existing fences) would have been reduced by 4 times. Reduction of danger due to the mitigation actions is also present in Degotalls series, but together with so many other effects it is difficult to be able to clearly identify it and to assess it quantitatively.

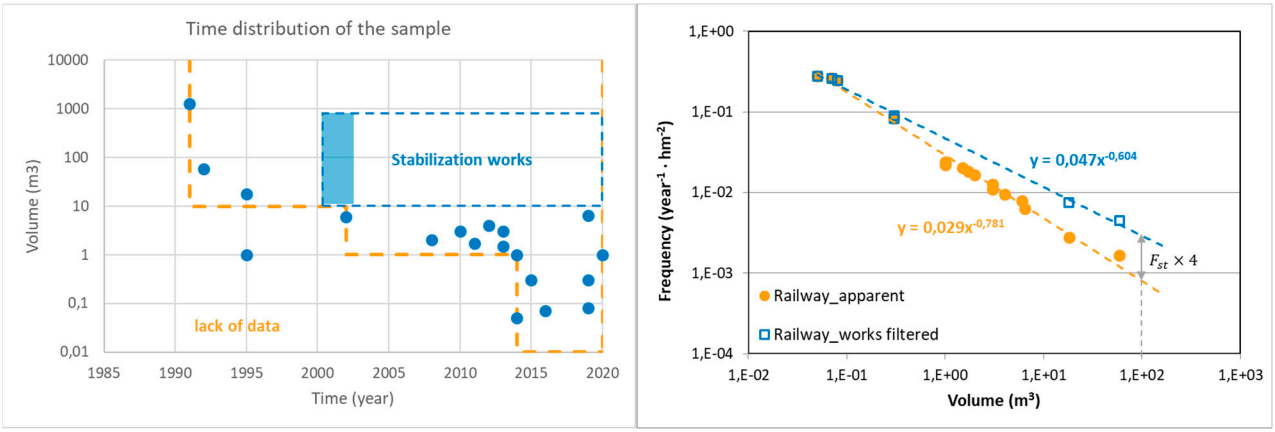

Figure S3. McF analysis for Rack Railway region in Montserrat Massif. On the left side, time distribution of the rockfall events recorded in the inventory, where those considered are delimited, and the effect of stabilization works on rockfall activity is highlighted. On the right side, resulting McF adjustments give an assessment of this effect.

References

1. Budetta P, Nappi M. Comparison between qualitative rockfall risk rating systems for a road affected by high traffic intensity. Nat Hazards Earth Syst Sci. 2013;13(6):1643–53.
2. Melzner S, Rossi M, Guzzetti F. Impact of mapping strategies on rockfall frequency-size distributions. Eng Geol [Internet]. 2020;272(March):105639. Available from: https://doi.org/10.1016/j.enggeo.2020.105639
3. Guerin A, Stock GM, Radue MJ, Jaboyedoff M, Collins BD, Matasci B, et al. Quantifying 40 years of rockfall activity in Yosemite Valley with historical Structure-from-Motion photogrammetry and terrestrial laser scanning. Geomorphology [Internet]. 2020;356(February):107069. Available from: https://doi.org/10.1016/j.geomorph.2020.107069
4. Žabota B, Kobal M. A new methodology for mapping past rockfall events: From mobile crowdsourcing to rockfall simulation validation. ISPRS Int J Geo-Information. 2020;9(9).
5. Juang CS, Stanley TA, Kirschbaum DB. Using citizen science to expand the global map of landslides: Introducing the cooperative open online landslide repository (COOLR). PLoS One. 2019;14(7):1–28.
6. Can R, Kocaman S, Gokceoglu C. A convolutional neural network architecture for auto-detection of landslide photographs to assess citizen science and volunteered geographic information data quality. ISPRS Int J Geo-Information. 2019;8(7).
7. Notti D, Guenzi D, Lasaponara R, Giordan D. Merging Historical Archives with Remote Sensing Data : A Methodology to Improve Rockfall Mitigation Strategy for Small Communities. Land. 2022;11(1951).
8. Scavia C, Barbero M, Castelli M, Marchelli M, Peila D, Torsello G, et al. Evaluating rockfall risk: Some critical aspects. Geosciences. 2020;10(3):1–30.
9. Royán MJ, Vilaplana JM. Distribución espacio-temporal de los desprendimientos de rocas en la Montaña de Montserrat. Cuaternario y Geomorfol. 2012;26(1–2):151–70.

10. Guerin A, Abellán A, Matasci B, Jaboyedoff M, Derron MH, Ravanel L. Brief communication: 3-D reconstruction of a collapsed rock pillar from Web-retrieved images and terrestrial lidar data-the 2005 event of the west face of the Drus (Mont Blanc massif). Nat Hazards Earth Syst Sci. 2017;17(7):1207–20.
11. Williams JG, Rosser NJ, Hardy RJ, Brain MJ, Afana AA. Optimising 4-D surface change detection: An approach for capturing rockfall magnitude-frequency. Earth Surf Dyn. 2018;6(1):101–19.
12. Vilajosana I, Suriñach E, Abellán A, Khazaradze G, Garcia D, Llosa J. Rockfall induced seismic signals: case study in Montserrat, Catalonia. Nat Hazards Earth Syst Sci. 2008;8(4):805–12.
13. Le Roy G, Helmstetter A, Amitrano D, Guyoton F, Le Roux-Mallouf R. Seismic Analysis of the Detachment and Impact Phases of a Rockfall and Application for Estimating Rockfall Volume and Free-Fall Height. J Geophys Res Earth Surf. 2019;124(11):2602–22.
14. Domènech G, Corominas J, Mavrouli O, Merchel S, Abellán A, Pavetich S, et al. Calculation of the rockwall recession rate of a limestone cliff, affected by rockfalls, using cosmogenic chlorine-36. Case study of the Montsec Range (Eastern Pyrenees, Spain). Geomorphology [Internet]. 2016; Available from: http://dx.doi.org/10.1016/j.geomorph.2017.04.005
15. Gallach X, Perrette Y, Lafon D, Chalmin É, Deline P, Ravanel L, et al. A new method for dating the surface exposure age of granite rock walls in the Mont Blanc massif by reflectance spectroscopy. Quat Geochronol [Internet]. 2021;101156. Available from: https://doi.org/10.1016/j.quageo.2021.101156
16. Corona C, Lopez-Saez J, Favillier A, Mainieri R, Eckert N, Trappmann D, et al. Modeling rockfall frequency and bounce height from three-dimensional simulation process models and growth disturbances in submontane broadleaved trees. Geomorphology [Internet]. 2017;281(December 2016):66–77. Available from: http://dx.doi.org/10.1016/j.geomorph.2016.12.019
17. Perret S, Stoffel M, Kienholz H. Spatial and temporal rockfall activity in a forest stand in the Swiss Prealps - A dendrogeomorphological case study. Geomorphology. 2006;74(1–4):219–31.
18. Chapot MS, Sohbati R, Murray AS, Pederson JL, Rittenour TM. Constraining the age of rock art by dating a rockfall event using sediment and rock-surface luminescence dating techniques. Quat Geochronol [Internet]. 2012;13:18–25. Available from: http://dx.doi.org/10.1016/j.quageo.2012.08.005
19. Lang A, Moya J, Corominas J, Schrott L, Dikau R. Classic and new dating methods for assessing the temporal occurrence of mass movements. Geomorphology. 1999;30(1–2):33–52.
20. Hantz D, Frayssines M. Rock wall retreat and historical back analysis of failures in Alpine limestone cliffs. In: Landslide processes: From geomorphologic mapping to dynamic modelling. Strasbourg; 2009. p. 125–9.
21. Hantz D, Benedetti L, Bourlès D, Carcaillet J. Un modèle de recul des falaises pour évaluer les fréquences d'éboulement. In: Journées Nationales de Géotechnique et de Géologie de l'Ingénieur 2012 [Internet]. Bordeaux, France; 2012. p. 845–52. Available from: https://hal.archives-ouvertes.fr/hal-00808588
22. Corominas J, Moya J. A review of assessing landslide frequency for hazard zoning purposes. Eng Geol [Internet]. 2008;102(3–4):193–213. Available from: http://dx.doi.org/10.1016/j.enggeo.2008.03.018
23. Hantz D, Colas B, Dewez T, Lévy C, Rossetti J-P, Guerin A, et al. Caractérisation quantitative des aléas rocheux de départ diffus. Rev Française Géotechnique. 2020;(163):2.
24. Corominas J, Mavrouli O, Ruiz-Carulla R. Magnitude and frequency relations: are there geological constraints to the rockfall size? Landslides. 2018;15(5):829–45.
25. Moos C, Bontognali Z, Dorren L, Jaboyedoff M, Hantz D. Estimating rockfall release scenarios based on a simple rockfall frequency model. In: Rock Slope Stability Symposium RSS-5. Chambéry (France); 2021.
26. Hantz D, Ventroux Q, Rossetti JP, Berger F. A new approach of diffuse rockfall hazard. In: Aversa S, Cascini L, Picarelli L, Scavia C, editors. Landslides and Engineered Slopes Experience, Theory and Practice. Napoli: CRC Press; 2016. p. 1063–7.
27. Ruiz-Carulla R, Corominas J, Mavrouli O. A methodology to obtain the block size distribution of fragmental rockfall deposits. Landslides [Internet]. 2015;12(4):815–25. Available from: http://link.springer.com/10.1007/s10346-015-0600-7
28. Ruiz-Carulla R, Corominas J. Analysis of Rockfalls by Means of a Fractal Fragmentation Model. Vol. 53, Rock Mechanics and Rock Engineering. 2020. 1433–1455 p.
29. Abellán A, Vilaplana JM, Calvet J, García-Sellés D, Asensio E. Rockfall monitoring by Terrestrial Laser Scanning - Case study of the basaltic rock face at Castellfollit de la Roca (Catalonia, Spain). Nat Hazards Earth Syst Sci. 2011;
30. Janeras M, Navarro M, Arnó G, Ruiz A, Kornus W, Talaya J, et al. LiDAR applications to rock fall hazard assesment in Vall de Núria. In: 4th ICA Mountain Cartography Workshop. Vall de Núria: ICA; 2004.
31. Abellán A, Calvet J, Vilaplana JM, Blanchard J. Detection and spatial prediction of rockfalls by means of terrestrial laser scanner monitoring. Geomorphology [Internet]. 2010;119(3–4):162–71.
32. Abellán A. Improvements in Our Understanding of Rockfall Phenomenon by Terrestrial Laser Scanning: Emphasis on Change Detection and Its Application to Spatial Prediction. Universitat de Barcelona; 2009.
33. Royán MJ. Caracterización y predicción de desprendimientos de rocas mediante LiDAR Terrestre. Universitat de Barcelona; 2015.
34. Blanch Gorriz X. Developing advanced photogrammetric methods for automated rockfall monitoring. Universitat de Barcelona; 2022.
35. Blanco L. Afloraments fracturats digitalitzats. Avaluació de les tècniques remotes en models DFN i aplicació de Machine Learning. Universitat de Barcelona; 2023.
36. Rocha M, Aisenstein B, Call R, Cording E, Franciss F, Franklin J, et al. Basic geotechnical description of rock masses. Int J Rock Mech Min Sci. 1981;18(1):85–110.
37. Abellán A, Jaboyedoff M, Oppikofer T, Vilaplana JM. Detection of millimetric deformation using a terrestrial laser scanner: experiment and application to a rockfall event. Nat Hazards Earth Syst Sci. 2009;9:365–72.
38. Matas G, Prades A, Núñez-Andrés MA, Buill F, Lantada N. Implementation of a fixed-location time lapse photogrammetric rock slope monitoring system in Castellfollit de la Roca, Spain. In: Joint International Symposium on Deformation Monitoring (JISDM). Valencia; 2022.
39. Núñez-Andrés MA, Prades-valls A, Matas G, Buill F, Lantada N. New Approach for Photogrammetric Rock Slope Premonitory Movements Monitoring. Remote Sens. 2023;15(293).
40. Royán MJ, Vilaplana JM, Janeras M, Abellán A. Detección e inventario de desprendimientos de rocas mediante el seguimiento con LiDAR Terrestre en la Montaña de Montserrat (Catalunya, España). XIV Reun Nac Geomorfol. 2016;

41. Royán MJ, Vilaplana JM, Abellán A. Towards rockfall prediction : Linking pre-failure deformation with precursory rockfall events. In: Alejano, Perucho, Olalla, Jiménez, editors. Rock Engineering and Rock Mechanics: Structures in and on Rock Masses. Taylor & Francis Group; 2014. p. 959–63.
42. Schütz M, Ohrhallinger S, Wimmer M. Fast Out-of-Core Octree Generation for Massive Point Clouds. Comput Graph Forum. 2020;39(7):155–67.
43. Pedraza O, Janeras M, Gili JA, Struth L, Buill F, Guinau M, et al. Comunicación de la geoinformación 3D mediante visores web y entornos inmersivos de rrealidad mixta en problemas de taludes y laderas. In: Hürlimann M, Pinyol N, editors. X Simposio Nacional sobre Taludes y Laderas Inestables. Granada, Spain: CIMNE; 2022.
44. Janeras M, Roca J, Gili JA, Pedraza O, Magnusson G, Núñez-Andrés MA, et al. Using Mixed Reality for the Visualization and Dissemination of Complex 3D Models in Geosciences—Application to the Montserrat Massif (Spain). Geosci. 2022;12(10).
45. Palau J, Janeras M, Prat E, Pons J, Ripoll J, Martínez P, et al. Preliminary assessment of rockfall risk mitigation in access infrastructures to Montserrat. In: Second World Landslide Forum. Rome; 2011.